



**HAL**  
open science

# Design, Synthesis, and Characterization of Carbon-Supported $\beta$ -Ni(OH)<sub>2</sub> Nanosheets for Miniaturized Nickel–Metal Hydride Batteries

Sho Fujita, Stève Baranton, Christophe Coutanceau, Gregory Jerkiewicz

## ► To cite this version:

Sho Fujita, Stève Baranton, Christophe Coutanceau, Gregory Jerkiewicz. Design, Synthesis, and Characterization of Carbon-Supported  $\beta$ -Ni(OH)<sub>2</sub> Nanosheets for Miniaturized Nickel–Metal Hydride Batteries. *Energy Technology*, 2024, 10.1002/ente.202301268 . hal-04403585

**HAL Id: hal-04403585**

**<https://hal.science/hal-04403585v1>**

Submitted on 18 Jan 2024

**HAL** is a multi-disciplinary open access archive for the deposit and dissemination of scientific research documents, whether they are published or not. The documents may come from teaching and research institutions in France or abroad, or from public or private research centers.

L'archive ouverte pluridisciplinaire **HAL**, est destinée au dépôt et à la diffusion de documents scientifiques de niveau recherche, publiés ou non, émanant des établissements d'enseignement et de recherche français ou étrangers, des laboratoires publics ou privés.

# Design, Synthesis, and Characterization of Carbon-Supported $\beta$ -Ni(OH)<sub>2</sub> Nanosheets for Miniaturized Nickel–Metal Hydride Batteries

Sho Fujita, Stève Baranton, Christophe Coutanceau,\* and Gregory Jerkiewicz\*


Carbon-supported  $\beta$ -Ni(OH)<sub>2</sub> nanosheets are prepared for miniaturized nickel–metal hydride batteries. The nanomaterial consists of thin and unfolded nanosheets, which possess a hexagonal crystallographic structure. Its unique structure gives rise to a remarkable specific capability, with 81.5% of the nanomaterial being used in electrical energy storage. Repetitive charge–discharge cycling between charge and discharge cut-off potentials ( $E_{\text{cut-off,ch}} = 1.50$  or  $1.65$  V and  $E_{\text{cut-off,dis}} = 1.20$  V) in aqueous NaOH solution is performed to examine the nanomaterial's specific charge and stability. The results show that the specific capacity gradually decreases upon repetitive charge–discharge cycling but still maintains a significant percentage of its initial value, 54% for  $E_{\text{cut-off,ch}} = 1.50$  V and 43% for  $E_{\text{cut-off,ch}} = 1.65$  V. A transmission electron microscopy analysis of the nanomaterial after the charge–discharge cycling demonstrates that the  $\beta$ -Ni(OH)<sub>2</sub> nanosheets are less-organized and distorted. The structural and morphological changes give rise to new features in cyclic voltammetry profiles and charge–discharge curves, and a decrease in the specific capacity of the nanomaterial. The degradation of the specific capacity is attributed to a loss of the initial structure, a reduction of the number of anchoring sites, and weakening of the bond between the  $\beta$ -Ni(OH)<sub>2</sub> nanosheets and the carbon support.

## 1. Introduction

In recent years, considerable efforts have been dedicated to improvement and renewal of the energy infrastructure to

S. Fujita, G. Jerkiewicz  
Department of Chemistry  
Queen's University  
90 Bader Lane, Kingston, Ontario K7L 3N6, Canada  
E-mail: gregory.jerkiewicz@queensu.ca

S. Baranton, C. Coutanceau  
IC2MP, UMR CNRS 7285  
Université de Poitiers  
4 rue Michel Brunet, TSA 51106, 86073 Poitiers Cedex 9, France  
E-mail: christophe.coutanceau@univ-poitiers.fr

 The ORCID identification number(s) for the author(s) of this article can be found under <https://doi.org/10.1002/ente.202301268>.

© 2024 The Authors. Energy Technology published by Wiley-VCH GmbH. This is an open access article under the terms of the Creative Commons Attribution-NonCommercial-NoDerivs License, which permits use and distribution in any medium, provided the original work is properly cited, the use is non-commercial and no modifications or adaptations are made.

DOI: 10.1002/ente.202301268

efficiently integrate and utilize energy originating from renewable sources.<sup>[1–3]</sup> Within this context, energy storage systems have received significant attention because of their ability to store renewable energy, and a large number of studies have reported on the development of small and large-scale energy storage systems.<sup>[4–6]</sup> For aqueous alkaline energy storage applications, nickel (Ni) is widely employed as an active electrode material and is normally present as a hydroxide.<sup>[7–12]</sup> There are two different nickel hydroxides, namely,  $\alpha$ -Ni(OH)<sub>2</sub> and  $\beta$ -Ni(OH)<sub>2</sub>.  $\beta$ -Ni(OH)<sub>2</sub> is the most common species that has a layered structure, which is comprised of Ni<sup>2+</sup> cations in a hexagonal planar arrangement and hydroxyl anions (OH<sup>−</sup>), with the oxygen atoms occupying the octahedral coordination site of each Ni<sup>2+</sup> (Figure 1). Intercalation of water molecules or foreign anions (e.g., nitrate) in between the nickel hydroxide layers increases the distance between the nickel hydroxide layers and modifies their stacking order, resulting in the formation of

$\alpha$ -Ni(OH)<sub>2</sub>.<sup>[13,14]</sup> Thus,  $\alpha$ -Ni(OH)<sub>2</sub> reveals a lower degree of crystallinity as compared to  $\beta$ -Ni(OH)<sub>2</sub>, which in turn has a well-defined crystallographic structure.<sup>[15]</sup>

According to the Bode scheme (Figure 2),  $\alpha$ -Ni(OH)<sub>2</sub> and  $\beta$ -Ni(OH)<sub>2</sub> transform into  $\gamma$ -NiOOH and  $\beta$ -NiOOH, respectively, upon oxidation in aqueous alkaline solutions.<sup>[16]</sup>  $\beta$ -NiOOH has a well-defined crystallographic structure as compared to  $\gamma$ -NiOOH because only proton insertion takes place upon its formation from  $\beta$ -Ni(OH)<sub>2</sub>. In contrast,  $\gamma$ -NiOOH contains water molecules and alkali cations in its crystallographic structure and, consequently, has a large interlayer distance and disordered layer stacking. It has been reported that  $\alpha$ -Ni(OH)<sub>2</sub> and  $\gamma$ -NiOOH possess higher charge capacity and facilitate fast active ion (H<sup>+</sup>) transfer inside the material that is attributed to the inserted water molecules.<sup>[13,15,17]</sup> Despite these properties possessed by  $\alpha$ -Ni(OH)<sub>2</sub> and  $\gamma$ -NiOOH, it is  $\beta$ -Ni(OH)<sub>2</sub> that has been preferably employed in practical applications due to its remarkable stability and cyclability. It is important to add that  $\alpha$ -Ni(OH)<sub>2</sub> undergoes chemical aging in aqueous alkaline solution that eventually produces  $\beta$ -Ni(OH)<sub>2</sub>,<sup>[14,17]</sup> and  $\gamma$ -NiOOH transforms to  $\beta$ -Ni(OH)<sub>2</sub> upon reduction.<sup>[13]</sup>

Nanostructured nickel hydroxides/oxyhydroxides reveal different structural and electrochemical properties compared to their

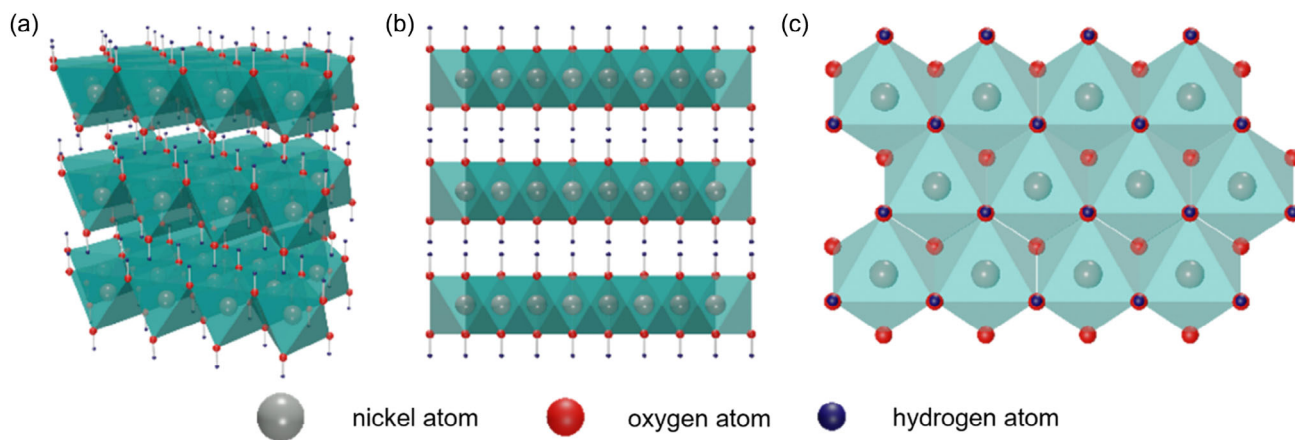


Figure 1. a) Visual representation of the structure of  $\beta$ -Ni(OH)<sub>2</sub> with b) side and c) top views.

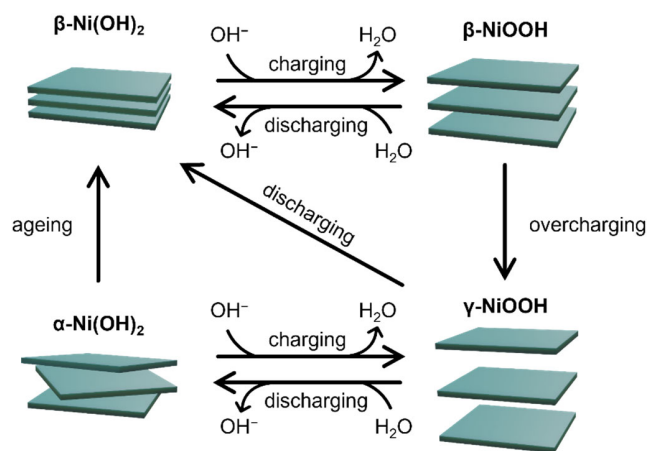


Figure 2. An overview of the transformations between different phases of Ni(OH)<sub>2</sub> and NiOOH.

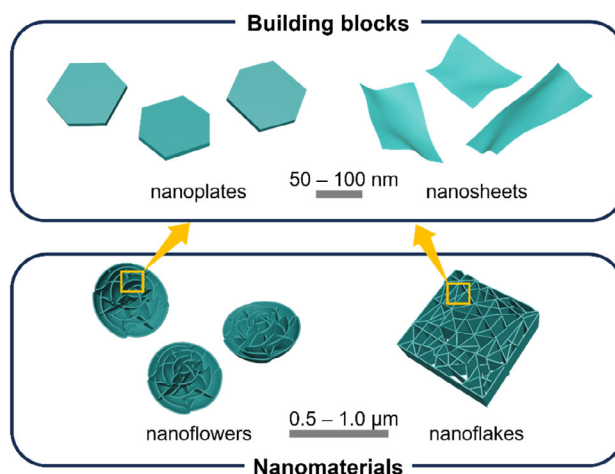


Figure 3. Visual representation of nickel hydroxide/oxyhydroxide nanoplates and nanosheets, as nanoscopic building blocks, and nanoflowers and nanoflakes synthesized using nanoplates and nanosheets.

bulk analogues, such as modification of their charge storage and activity toward the oxygen evolution reaction (OER) and the oxygen reduction reaction (ORR).<sup>[18–20]</sup> There are several reports describing successful design and synthesis of various nickel hydroxide nanomaterials, such as nanoflakes,<sup>[21–24]</sup> nanoflowers,<sup>[25–28]</sup> single-crystalline nanoplates,<sup>[29–32]</sup> and nanosheets.<sup>[33,34]</sup> It is important to emphasize that nickel hydroxide/oxyhydroxide nanoflakes and nanoflowers are made from respective nanoplates or nanosheets, which act as building blocks (Figure 3). Nickel hydroxide/oxyhydroxide nanoflakes and nanoflowers exhibit a large surface area as compared to bulk materials (e.g., nickel hydroxide/oxyhydroxide particles), resulting in an increase in the number of active surface sites and shorter proton transport pathways. Consequently, these structural features lead to an enhancement of their charge capacity, cyclability, and charge–discharge rate capability.<sup>[23,24,26]</sup> It is important to add that nanoflakes and nanoflowers require a substrate for their preparation, whereas nanoplates and nanosheets do not. Thus, nickel hydroxide/oxyhydroxide nanoplates and nanosheets might be more suitable for large-scale electrode preparation, because their synthesis is easily scalable.<sup>[31,33,34]</sup> In the case of nickel

hydroxide/oxyhydroxide nanoplates, each nanoplate possesses single crystallographic structure and, thus, facilitates fast proton transport inside the nanomaterial, enhancing its charge–discharge rate capability and cyclability.<sup>[32]</sup> Nickel hydroxide/oxyhydroxide nanosheets possess a quasi-three-dimensional structure and are very thin (they are thinner than nanoplates). These properties reduce the length of pathways for proton and electron transports inside the nanosheets, as well as offer a high surface-to-volume ratio.<sup>[33]</sup> Thus, nickel hydroxide/oxyhydroxide nanosheets reveal a high charge capacity, a high charge–discharge rate capability, and extended cyclability.<sup>[34]</sup> The above mentioned properties of various nickel hydroxide/oxyhydroxide nanomaterials make them suitable candidates for aqueous alkaline electrochemical energy storage and generation applications.

Bearing in mind that nanostructured nickel hydroxide/oxyhydroxide materials offer various benefits, it is important to investigate their characteristics and performance in relation to their application in the next generation of aqueous alkaline

energy storage systems.<sup>[35,36]</sup> For instance, it has been reported that  $\beta$ -Ni(OH)<sub>2</sub> nanoparticles (NPs) with an average size of 2–3 nm have a core-shell structure and demonstrate remarkable stability upon repetitive potential cycling.<sup>[37]</sup> These NPs were proposed as a cathode material for miniaturized nickel–metal hydride (Ni–MH) batteries, with octahedral Pd NPs used as an anode material.<sup>[38]</sup> In general, Ni–MH batteries are one of the most common alkaline batteries found in automotive and stationary applications due to their remarkable safety and reliability, although they are heavy, thus offer low energy density.<sup>[39–41]</sup> The application of Pd as a hydrogen storage material for battery applications is not common due to its high cost and limited supplies. However, the envisaged Ni–PdH batteries employing  $\beta$ -Ni(OH)<sub>2</sub> NPs and octahedral Pd NPs are being designed with miniaturized energy storage applications in mind, such as small-scale electronics, or other applications where the cost is of secondary importance to the required dependability.<sup>[38]</sup>

In this study, carbon-supported  $\beta$ -Ni(OH)<sub>2</sub> nanosheets were synthesized using a water-in-oil microemulsion method for the envisaged application in miniaturized Ni–MH batteries. First,  $\beta$ -Ni(OH)<sub>2</sub> NPs were synthesized and characterized, and then assembled into  $\beta$ -Ni(OH)<sub>2</sub> nanosheets. The chemical composition of the carbon-supported  $\beta$ -Ni(OH)<sub>2</sub> nanosheets and Ni loading was examined by thermogravimetric analysis (TGA). The structure and morphology of the  $\beta$ -Ni(OH)<sub>2</sub> NPs and the carbon-supported  $\beta$ -Ni(OH)<sub>2</sub> nanosheets were examined by transmission electron microscopy (TEM). The crystallographic structure of the carbon-supported  $\beta$ -Ni(OH)<sub>2</sub> nanosheets was determined by acquiring and analyzing X-ray diffraction (XRD) patterns. Cyclic voltammetry (CV) and chronopotentiometry (CP)

measurements were conducted to examine the charge and discharge behavior as well as to analyze long-term stability (cyclability) of the nanomaterial. Because repetitive charge–discharge cycling of electrochemical energy materials is known to introduce structural changes, the structure of the carbon-supported  $\beta$ -Ni(OH)<sub>2</sub> nanosheets was examined using TEM after repetitive charge–discharge cycling.

## 2. Results and Discussion

### 2.1. Physicochemical Characterizations

TEM images of the  $\beta$ -Ni(OH)<sub>2</sub> NPs are shown in **Figure 4a,b** and reveal that the  $\beta$ -Ni(OH)<sub>2</sub> NPs are dispersed and possess a well-defined almost spherical shape. The spacing between the lattice fringes presented in Figure 4b is found to be 0.236 nm, which corresponds to the (101) set of lattice planes of  $\beta$ -Ni(OH)<sub>2</sub>.<sup>[37]</sup> Figure 4c presents a histogram of the particle size distribution acquired by measuring the sizes of 300  $\beta$ -Ni(OH)<sub>2</sub> NPs; the results indicate that the average NP size was 5.3 nm. The TEM images of the carbon-supported  $\beta$ -Ni(OH)<sub>2</sub> nanosheets (Figure 4d,e) reveal that the nanomaterial possesses an unfolded sheet structure. In addition, the TEM images allow us to conclude that the nanosheets are very thin because we are able to observe needle-like structures that correspond to the edges of the nanosheets. In the Experimental Section (“Preparation of Unsupported  $\beta$ -Ni(OH)<sub>2</sub> NPs and Carbon-Supported  $\beta$ -Ni(OH)<sub>2</sub> Nanosheets”), it is mentioned that the synthesized  $\beta$ -Ni(OH)<sub>2</sub> NPs were stored in isopropanol and remained stable and dispersed (nonaggregated) for extended periods of time. The

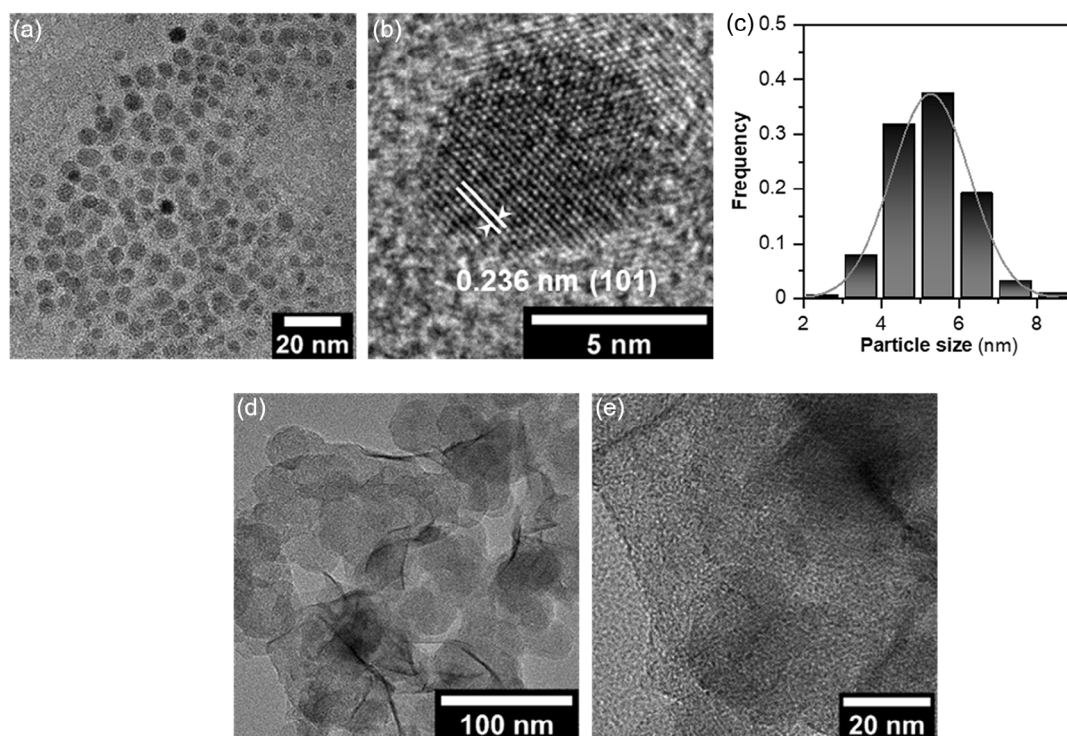


**Figure 4.** a,b) TEM images of a collection of  $\beta$ -Ni(OH)<sub>2</sub> NPs and c) a histogram of their size distribution. d,e) TEM images of the carbon-supported  $\beta$ -Ni(OH)<sub>2</sub> nanosheets.

synthesis of the carbon-supported  $\beta$ -Ni(OH)<sub>2</sub> nanosheets involved an addition of the carbon support (the step 2 in the flow chart shown in “Preparation of Unsupported  $\beta$ -Ni(OH)<sub>2</sub> NPs and Carbon-Supported  $\beta$ -Ni(OH)<sub>2</sub> Nanosheets”) and additional rinsing of the nanomaterial using ultra-high purity (UHP) water (the step 3 in the flow chart shown in “Preparation of Unsupported  $\beta$ -Ni(OH)<sub>2</sub> NPs and Carbon-Supported  $\beta$ -Ni(OH)<sub>2</sub> Nanosheets”). Bearing in mind the stability of the unsupported  $\beta$ -Ni(OH)<sub>2</sub> NPs in isopropanol, we propose that the  $\beta$ -Ni(OH)<sub>2</sub> NPs spontaneously organize into nanosheets on the carbon support during the rinsing step with UHP water. This rinsing step was accompanied by the formation of gas bubbles. The evolved H<sub>2</sub>(g) was due to the reaction between the remaining (unreacted) NaBH<sub>4</sub> used in the nickel precursor reduction step and the UHP water. The reaction between NaBH<sub>4</sub> and UHP water (hydrolysis of NaBH<sub>4</sub>) locally changed the pH of the aqueous solution making it slightly alkaline. As it is explained elsewhere, aqueous alkaline solutions facilitate the transformation of  $\beta$ -Ni(OH)<sub>2</sub> NPs into more complex  $\beta$ -Ni(OH)<sub>2</sub> structures.<sup>[42,43]</sup>

The crystallographic structure and chemical composition of the carbon-supported  $\beta$ -Ni(OH)<sub>2</sub> nanosheets were investigated by XRD, and an XRD pattern of the carbon support was also recorded and facilitated the interpretation of the experimental results (Figure 5). The peak deconvolution for each diffraction pattern was performed using pseudo-Voigt function with the Levenberg–Marquardt method on the Fityk software.<sup>[44]</sup> The

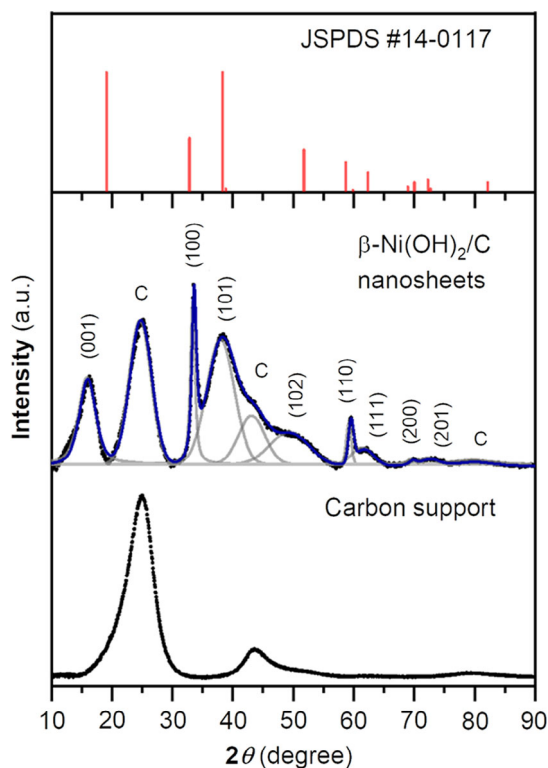


**Figure 5.** XRD patterns of the carbon-supported  $\beta$ -Ni(OH)<sub>2</sub> nanosheets and the carbon support. A fitting line was obtained for the XRD pattern of the carbon-supported  $\beta$ -Ni(OH)<sub>2</sub> nanosheets using deconvoluted peaks that correspond to  $\beta$ -Ni(OH)<sub>2</sub> (indicated with lattice planes) and the graphite of the carbon support (indicates as “C”).

results of the curve fitting indicate that the XRD pattern for the carbon-supported  $\beta$ -Ni(OH)<sub>2</sub> nanosheets is composed of diffraction peaks associated with the  $\beta$ -Ni(OH)<sub>2</sub> species and those with graphitic structure of the carbon support. The  $\beta$ -Ni(OH)<sub>2</sub> diffraction peaks appear at  $2\theta = 15.96^\circ, 33.58^\circ, 38.14^\circ, 49.63^\circ, 59.60^\circ, 61.78^\circ, 69.81^\circ,$  and  $72.72^\circ$ , confirm that the  $\beta$ -Ni(OH)<sub>2</sub> nanosheets have a hexagonal structure (JCPDS 14-0117). The graphite of the carbon support diffraction peaks at  $2\theta = 24.77^\circ, 43.42^\circ,$  and  $80.02^\circ$  are consistently observed in the cases of the carbon-supported  $\beta$ -Ni(OH)<sub>2</sub> nanosheets and the support material. In our previous report, the presence of NiO was proposed on the basis of the XRD pattern of similarly prepared carbon-supported  $\beta$ -Ni(OH)<sub>2</sub> NPs. However, in this study, we found that the diffraction peaks of the carbon support appear at the same diffraction angles as those for the NiO (e.g.,  $2\theta = 43.42^\circ$  and  $80.02^\circ$ ). The previous report also showed a diffraction peak assigned to the (111) plane of NiO at  $2\theta = 36.13^\circ$ ,<sup>[37]</sup> but this peak is not observed in the current XRD analysis. Thus, the XRD pattern of the carbon-supported  $\beta$ -Ni(OH)<sub>2</sub> nanosheets indicates that they possess a homogeneous  $\beta$ -Ni(OH)<sub>2</sub> phase without any NiO. It is important to add that NiO could be formed as a minor phase (e.g., at the surface of the nanosheets) during the heat treatment, but this nickel oxide is expected to convert back to the nickel hydroxide once the nanomaterial is in contact with aqueous alkaline solution during electrochemical characterization.

The actual mass of the  $\beta$ -Ni(OH)<sub>2</sub> nanosheets on the carbon support was examined by conducting TGA measurements and analyzing the mass variation as a function of rising temperature (Figure 6). The first derivative of the mass variation was calculated from the material mass loss with respect to the temperature. The mass variation curve demonstrates the following: 1) physisorbed water present on the surface of the  $\beta$ -Ni(OH)<sub>2</sub> nanosheets was evaporated (desorbed) between  $T = 293$  K and  $T = 480$  K, followed by dehydration of  $\beta$ -Ni(OH)<sub>2</sub> to NiO that occurred between  $T = 510$  K and  $T = 569$  K<sup>[45,46]</sup>; 2) subsequently the mass of the material dramatically decreases due to the combustion of the carbon support between  $T = 680$  K and  $T = 850$  K; 3) the mass

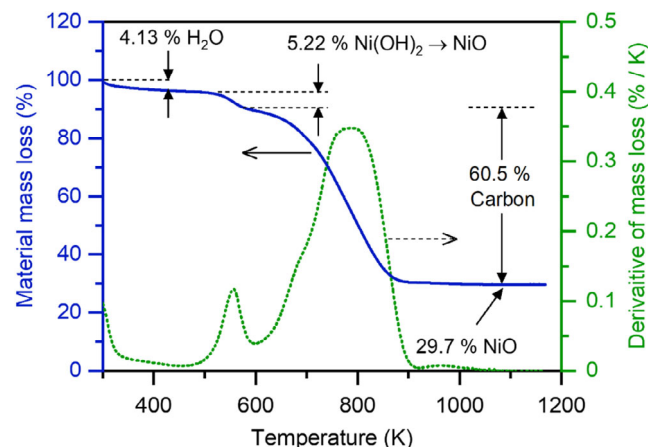


**Figure 6.** Change in the material mass (mass loss in % with respect to the initial sample mass; the blue curve) and the first derivative of the mass loss as a function of temperature (the dotted green curve) for the carbon-supported  $\beta$ -Ni(OH)<sub>2</sub> acquired by TGA analysis.



variation leveled off (the sample mass became constant) as there was only NiO (dehydrated form of the  $\beta$ -Ni(OH)<sub>2</sub>) remaining after the combustion of the carbon support. Using the mass of the remaining NiO ( $\approx 3.737$  mg), the nickel loading in the carbon-supported  $\beta$ -Ni(OH)<sub>2</sub> nanosheets was determined using the following equation:

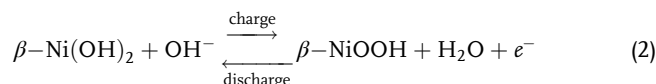
$$w_{\text{Ni}} = \frac{m_{\text{Ni}}}{m_{\text{Ni}} + m_{\text{C}}} \times 100 \quad (1)$$

where  $w_{\text{Ni}}$  is the nickel loading in the sample,  $m_{\text{Ni}}$  is the experimentally determined mass of nickel, and  $m_{\text{C}}$  is the experimentally determined mass of the carbon support. An analysis of the TGA results indicated that the nickel metal loading was 27.81 wt%, which is very close to the target value of 30 wt%.

## 2.2. Electrochemical Behavior of the Carbon-Supported $\beta$ -Ni(OH)<sub>2</sub> Nanosheets

The electrochemical behavior of the carbon-supported  $\beta$ -Ni(OH)<sub>2</sub> nanosheets in the potential range of the interconversions between  $\beta$ -Ni(OH)<sub>2</sub> and  $\beta$ -NiOOH was examined by conducting CV and CP experiments in 0.50 M aqueous NaOH solution at  $T = 293$  K. **Figure 7a** presents CV profiles in the 0.10–1.60 V range acquired at various potential scan rates, namely  $s = 1.00, 5.00, 10.0, 20.0, 50.0,$  and  $100 \text{ mV s}^{-1}$ . The results demonstrate the usual and well-defined anodic and cathodic peaks that correspond to the oxidation of  $\beta$ -Ni(OH)<sub>2</sub> and the reduction of  $\beta$ -NiOOH.<sup>[47]</sup> Because  $\beta$ -Ni(OH)<sub>2</sub> is employed in rechargeable

Ni–MH batteries, the interconversions represent charge (oxidation) and discharge (reduction) reactions (Equation (2)).



The CV profiles obtained for this nanomaterial reveal excellent reversibility of the redox reactions, thus demonstrating its potential as a practical electrode material. In general, the redox interconversions between  $\beta$ -Ni(OH)<sub>2</sub> and  $\beta$ -NiOOH are surface processes limited by the adsorption of OH<sup>−</sup> or a semi-infinite/finite-space diffusion process limited by the proton diffusion inside the  $\beta$ -Ni(OH)<sub>2</sub> species.<sup>[47]</sup> To determine which process controls the redox interconversions, logarithms of the oxidation and reduction peak currents ( $I_{\text{peak,ox}}$  and  $I_{\text{peak,red}}$ ) are plotted as a function of a logarithm of the potential scan rate  $s$  (Figure 7b). A linear relationship is observed for the entire range of the potential scan rate values for the oxidation of  $\beta$ -Ni(OH)<sub>2</sub> and the reduction of  $\beta$ -NiOOH with the respective slopes being 0.62 and 0.55, which indicate that the redox interconversions between the  $\beta$ -Ni(OH)<sub>2</sub> and  $\beta$ -NiOOH are under proton diffusion control inside the  $\beta$ -Ni(OH)<sub>2</sub> species (the oxidation of  $\beta$ -Ni(OH)<sub>2</sub> to  $\beta$ -NiOOH releases H<sup>+</sup> that diffuses across the hydroxide layer and combines with OH<sup>−</sup> to form H<sub>2</sub>O as it reaches the nanomaterial–electrolyte interface).<sup>[24]</sup>

Figure 7c presents charge–discharge (CP,  $E$  vs  $t$ ) curves obtained at different current density values ( $j = 0.500, 1.00, 2.00, 5.00, 10.0,$  and  $20.0 \text{ A g}^{-1}$ ) for the carbon-supported

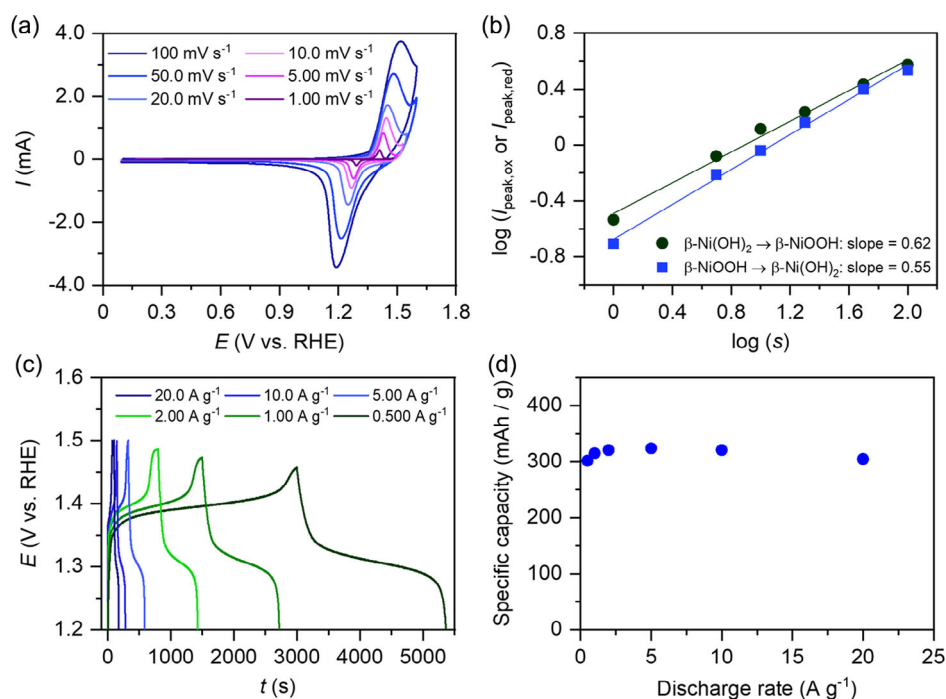


**Figure 7.** a) CV profiles for the carbon-supported  $\beta$ -Ni(OH)<sub>2</sub> nanosheets recorded at  $s = 1.00, 2.00, 5.00, 10.0, 20.0, 50.0,$  and  $100 \text{ mV s}^{-1}$  in 0.50 M aqueous NaOH solution at  $T = 293$  K. b) A logarithm of the oxidation and reduction peak currents ( $I_{\text{peak,ox}}$  and  $I_{\text{peak,red}}$ ) plotted as a function of a logarithm of the potential scan rate  $s$ . c) Charge–discharge curves for the carbon-supported  $\beta$ -Ni(OH)<sub>2</sub> nanosheets in 0.50 M aqueous NaOH solution at  $T = 293$  K acquired at  $j = 0.500, 1.00, 2.00, 5.00, 10.0,$  and  $20.0 \text{ A g}^{-1}$  with  $E_{\text{cut-off,ch}} = 1.50 \text{ V}$  and  $E_{\text{cut-off,dis}} = 1.20 \text{ V}$ . d) Evolution of the specific capacity of the carbon-supported  $\beta$ -Ni(OH)<sub>2</sub> nanosheets as a function of the discharge rate.

$\beta$ -Ni(OH)<sub>2</sub> nanosheets. In the case of a current density of  $j = 0.500 \text{ A g}^{-1}$ , there are plateau regions in both charge and discharge curves, and these regions correspond to the oxidation of  $\beta$ -Ni(OH)<sub>2</sub> and the reduction of  $\beta$ -NiOOH. Likewise, the charge and discharge curves obtained at the other (higher) current density values also present plateau regions, although they are less noticeable because the charge and discharge are completed in a shorter time. On the basis of these results, we were able to determine the specific capacity values for the carbon-supported  $\beta$ -Ni(OH)<sub>2</sub> nanosheets, which are presented in Figure 7d. As explained in the Experimental Section,  $E_{\text{cut-off, ch}} = 1.50 \text{ V}$  and  $E_{\text{cut-off, dis}} = 1.20 \text{ V}$ . The results demonstrate that the specific capacity has a nearly constant value (it does not depend on the value of the current density), thus pointing a remarkable charge–discharge rate capability of the nanomaterial that is not observed in the case of analogous bulk materials. This characteristic is attributed to the unique sheet-shaped structure of the nanomaterial that enhances the transfer of electrons and diffusion of protons, as well as offers a large surface area.<sup>[34]</sup> Furthermore, the experimentally determined maximum specific capacity of the carbon-supported  $\beta$ -Ni(OH)<sub>2</sub> nanosheets is  $334 \pm 10 \text{ mAh g}^{-1}$ , thus  $\approx 20\%$  higher than that of the carbon-supported  $\beta$ -Ni(OH)<sub>2</sub> NPs reported in our previous study.<sup>[37]</sup> The increase in the specific capacity of the carbon-supported  $\beta$ -Ni(OH)<sub>2</sub> nanosheets is attributed to the homogeneity of the nanomaterial that does not contain any NiO that otherwise would not participate in the redox interconversions between the  $\beta$ -Ni(OH)<sub>2</sub> and  $\beta$ -NiOOH (this conclusion is supported by our XRD data, Figure 5). It is important to add that if the entire sample of the  $\beta$ -Ni(OH)<sub>2</sub> nanosheets were converted to  $\beta$ -NiOOH, then the specific capacity would be  $410 \text{ mAh g}^{-1}$ . Thus, the experimentally determined value of  $334 \text{ mAh g}^{-1}$  corresponds to a remarkable 81.5% utilization of the material.

### 2.3. Stability and Charge–Discharge Characteristics of the Carbon-Supported $\beta$ -Ni(OH)<sub>2</sub> Nanosheets

Any eventual application of the carbon-supported  $\beta$ -Ni(OH)<sub>2</sub> nanosheets depends on several materials science and electrochemical characteristics, including their stability. Consequently,

the cyclability (long-term performance and stability) of the carbon-supported  $\beta$ -Ni(OH)<sub>2</sub> nanosheets was investigated by repetitive charge–discharge cycling with  $E_{\text{cut-off, ch}} = 1.50 \text{ V}$  and  $E_{\text{cut-off, dis}} = 1.20 \text{ V}$  at  $j = 80.0 \text{ A g}^{-1}$  in unpurified and purified  $0.50 \text{ M}$  aqueous NaOH solutions. The purified solution is used in this study because trace amounts of Fe remaining in the freshly-prepared alkaline solution can be incorporated into the crystallographic structure of  $\beta$ -Ni(OH)<sub>2</sub> and modify its electrocatalytic properties and enhance the OER activity.<sup>[15]</sup> The enhanced OER may interfere with the charging and, consequently, reduce the specific capacity of the nanomaterial. **Figure 8** presents an evolution of the specific capacity as a function of the number of repetitive charge–discharge cycles conducted in unpurified and purified aqueous alkaline solutions. The results reveal that the specific capacity of the carbon-supported  $\beta$ -Ni(OH)<sub>2</sub> nanosheets gradually decreases upon the charge–discharge cycling. As can be observed in the insets in Figure 8, the charge and discharge curves in unpurified and purified aqueous NaOH solutions present typical features characteristic of the  $\beta$ -Ni(OH)<sub>2</sub> oxidation and the subsequent reduction of  $\beta$ -NiOOH.<sup>[33,48]</sup> Since the charge and discharge curves in the unpurified and purified solutions exhibit the same shape and the specific capacity curves, they indicate that the presence of trace amounts of Fe in unpurified aqueous NaOH solution has no impact on the redox behavior of the carbon-supported  $\beta$ -Ni(OH)<sub>2</sub> nanosheets.

For a comparative analysis, **Figure 9a,b** presents CV profiles and Figure 9c,d charge–discharge curves for the carbon-supported  $\beta$ -Ni(OH)<sub>2</sub> nanosheets prior to and after the repetitive charge–discharge cycling performed in the unpurified and purified aqueous NaOH solutions. The CV profiles in the unpurified solution (Figure 9a) demonstrate that the anodic peak associated with the oxidation of  $\beta$ -Ni(OH)<sub>2</sub> shifts toward higher potentials after the repetitive charge–discharge cycling and an enhanced OER activity is observed, as indicated by a sharp increase in the current at  $E \geq 1.60 \text{ V}$ . As mentioned above, the enhancement of the OER is known to arise from the incorporation of Fe into the crystallographic structure of  $\beta$ -Ni(OH)<sub>2</sub>.<sup>[49]</sup> In contrast, the current of the cathodic peak associated with the reduction of  $\beta$ -NiOOH decreases after the repetitive charge–discharge cycling, thus indicating that the specific capacity of the carbon-supported  $\beta$ -Ni(OH)<sub>2</sub> nanosheets gradually decreases, which is in

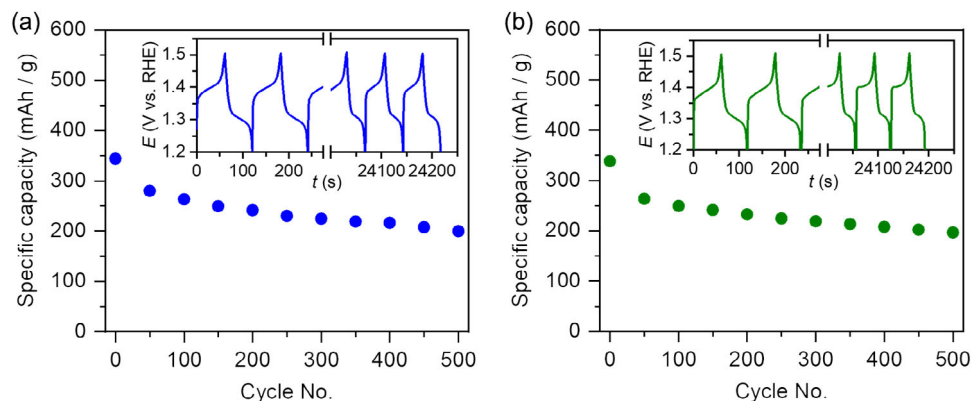


**Figure 8.** Evolution of the specific capacity of the carbon-supported  $\beta$ -Ni(OH)<sub>2</sub> nanosheets as a function of the number of repetitive charge–discharge cycles conducted in unpurified (graph a) and purified (graph b)  $0.50 \text{ M}$  aqueous NaOH solution at  $j = 80.0 \text{ A g}^{-1}$  and  $T = 293 \text{ K}$  with  $E_{\text{cut-off, ch}} = 1.50 \text{ V}$  and  $E_{\text{cut-off, dis}} = 1.20 \text{ V}$ . The insets present charge and discharge curves in the respective electrolyte solutions.

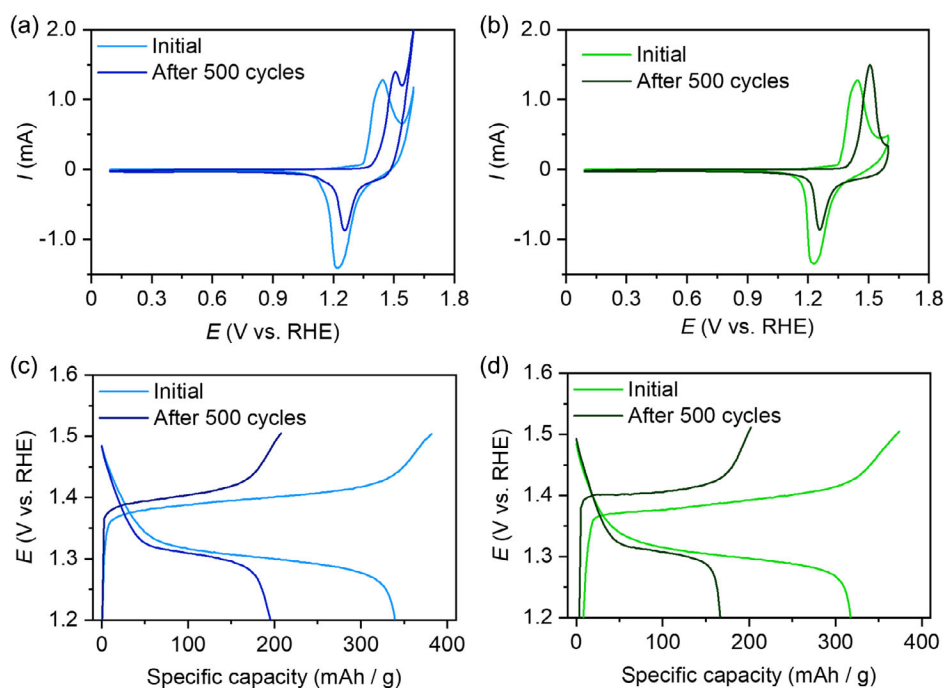


**Figure 9.** a,b) CV profiles and c,d) charge–discharge curves for the carbon-supported  $\beta$ -Ni(OH) $_2$  nanosheets acquired prior to and after repetitive charge–discharge cycling in unpurified (the blue transients) and purified (the green transients) 0.50 M aqueous NaOH solutions. The CV profiles were recorded at  $s = 20.0 \text{ mV s}^{-1}$  in the 0.10–1.60 V range and  $T = 293 \text{ K}$ . The charge–discharge cycling was conducted at  $j = 80.0 \text{ A g}^{-1}$  and  $T = 293 \text{ K}$  with  $E_{\text{cut-off, ch}} = 1.50 \text{ V}$  and  $E_{\text{cut-off, dis}} = 1.20 \text{ V}$ .

agreement with the results presented in Figure 8. In addition, the charge and discharge curves (Figure 9c) become shortened (the cut-off potential is reached faster) after the repetitive charge–discharge cycling, thus indicating that the specific capacity of the carbon-supported  $\beta$ -Ni(OH) $_2$  nanosheets decreased after the repetitive charge–discharge cycling. In the case of the purified aqueous NaOH solution, the CV profiles (Figure 9b) reveal a shift of the anodic peak toward higher potentials after the repetitive charge–discharge cycling but an enhancement of the OER is not observed. The current of the cathodic peak becomes smaller after the repetitive charge–discharge cycling, thus indicating a decrease in the specific capacity of the carbon-supported  $\beta$ -Ni(OH) $_2$  nanosheets. The charge and discharge curves in the purified solution (Figure 9d) also demonstrate that the specific capacity of the nanomaterial is reduced after the repetitive charge–discharge cycling, again in agreement with the results presented in Figure 8.

The results of the repetitive charge–discharge cycling conducted in the unpurified and purified aqueous alkaline solutions revealed that the specific capacity of the carbon-supported  $\beta$ -Ni(OH) $_2$  nanosheets gradually decreased with the increasing cycle number. Although in the case of the unpurified electrolyte solution, we observe an enhancement of the electrocatalytic activity toward the OER due to the incorporation of trace amounts of Fe in the  $\beta$ -Ni(OH) $_2$  nanosheets, this contaminant is not the cause of the reduction in the specific capacity. We propose that the loss of the specific capacity is due to structural changes within the  $\beta$ -Ni(OH) $_2$  nanosheets, which give rise to altered charging–discharging behavior. This proposal is supported by the CV

results, which show that the anodic peak shifted toward higher potentials and the cathodic peak became smaller after the repetitive charge–discharge cycling (Figure 9a,b). Details of the structural changes that develop during the repetitive charge–discharge cycling will be discussed in the following section.

In our previous study, we reported on the variation of the specific capacity of carbon-supported  $\beta$ -Ni(OH) $_2$  NPs upon repetitive cycling in the 0.05–1.75 V range (the NPs were reported to be randomly dispersed on the support and did not form any organized structures).<sup>[37]</sup> To relate our new results for the carbon-supported  $\beta$ -Ni(OH) $_2$  nanosheets to those for the  $\beta$ -Ni(OH) $_2$  NPs, the specific capacity of the carbon-supported  $\beta$ -Ni(OH) $_2$  nanosheets was examined by repetitive charge–discharge cycling conducted using an additional  $E_{\text{cut-off, ch}}$  value, namely  $E_{\text{cut-off, ch}} = 1.65 \text{ V}$  (the results for  $E_{\text{cut-off, ch}} = 1.50 \text{ V}$  are shown in Figure 7d, 8, and 9; in a later section, the selection of 1.65 V as  $E_{\text{cut-off, ch}}$  is justified). **Figure 10a** presents the variation of the specific capacity of the carbon-supported  $\beta$ -Ni(OH) $_2$  nanosheets in relation to the repetitive charge–discharge cycle number in unpurified 0.50 M aqueous NaOH solution; the cycling was performed at  $j = 80.0 \text{ A g}^{-1}$  with  $E_{\text{cut-off, ch}}$  being 1.50 and 1.65 V and  $E_{\text{cut-off, dis}} = 1.20 \text{ V}$ . In the case of  $E_{\text{cut-off, ch}} = 1.50 \text{ V}$ , the initial specific capacity is  $270 \pm 27 \text{ mAh g}^{-1}$  and gradually decreases to  $147 \pm 18 \text{ mAh g}^{-1}$ . In contrast, the initial specific capacity in the case of  $E_{\text{cut-off, ch}} = 1.65 \text{ V}$  is significantly higher and equals to  $327 \pm 33 \text{ mAh g}^{-1}$  and decreases to  $140 \pm 14 \text{ mAh g}^{-1}$  after 1000 charge–discharge cycles. Since the decrease in the specific capacity is greater in the case of  $E_{\text{cut-off, ch}} = 1.65 \text{ V}$  (43%) than in the case of  $E_{\text{cut-off, ch}} = 1.50 \text{ V}$  (54%), we may conclude that



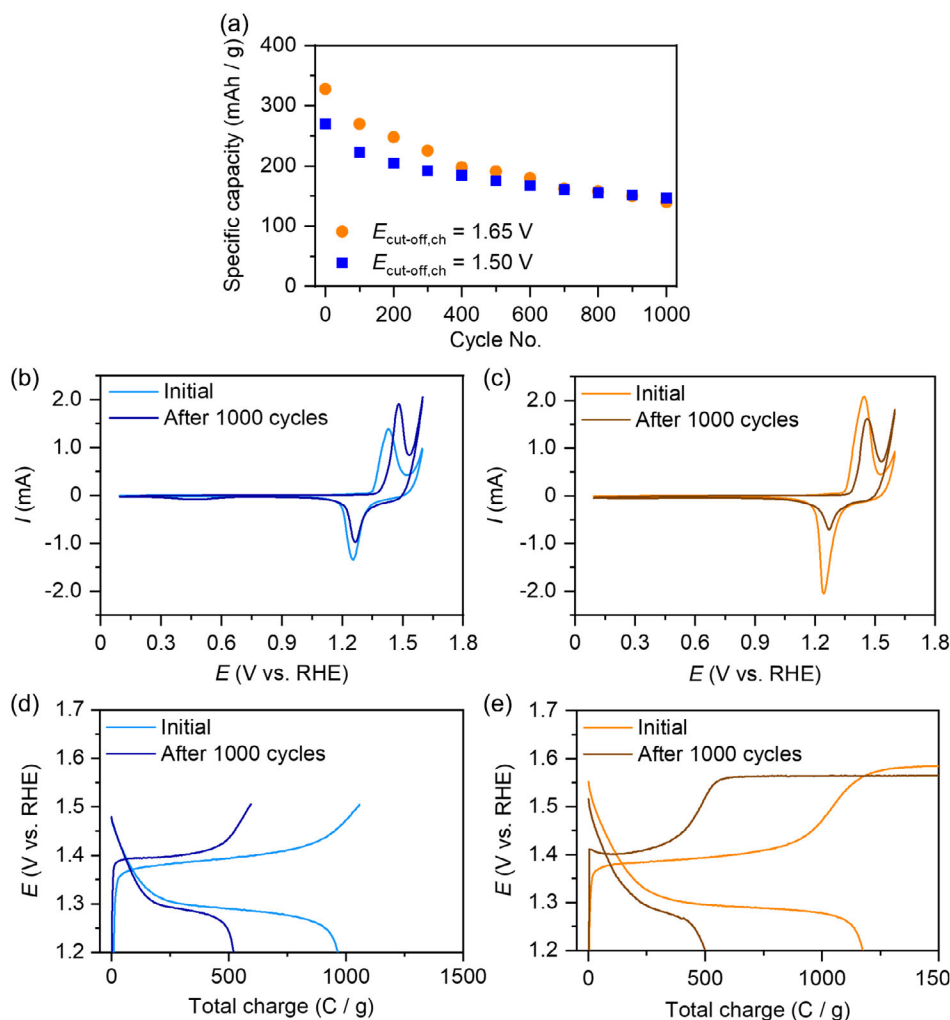


**Figure 10.** a) Evolution of the specific capacity of the carbon-supported  $\beta$ -Ni(OH)<sub>2</sub> nanosheets as a function of the number of charge–discharge cycle conducted at  $j = 80.0 \text{ A g}^{-1}$ . b,c) CV profiles for the carbon-supported  $\beta$ -Ni(OH)<sub>2</sub> nanosheets recorded at  $s = 20.0 \text{ mV s}^{-1}$  in the 0.10–1.60 V range acquired prior to and after the repetitive charge–discharge cycling. d,e) Charge and discharge curves recorded prior to and after the repetitive charge–discharge cycling. All the results were obtained in unpurified 0.50 M aqueous NaOH solution at  $T = 293 \text{ K}$ . In all charge–discharge cycles,  $E_{\text{cut-off, ch}} = 1.50 \text{ V}$  (the blue symbols, profiles, and transients),  $E_{\text{cut-off, ch}} = 1.65 \text{ V}$  (orange symbols, profiles, and transients), and  $E_{\text{cut-off, dis}} = 1.20 \text{ V}$ .

$E_{\text{cut-off, ch}} = 1.50 \text{ V}$  is favorable for charge retention (the charge retention is  $\approx 25\%$  higher than in the case of  $E_{\text{cut-off, ch}} = 1.65 \text{ V}$ ).

To analyze the change in the behavior of the redox interconversions between  $\beta$ -Ni(OH)<sub>2</sub> and  $\beta$ -NiOOH upon the repetitive charge–discharge cycling conducted with two  $E_{\text{cut-off, ch}}$  values, CV profiles were compared prior to and after the charge–discharge cycling (Figure 10b,c). Figure 10d,e presents relations between the potential adopted by the nanomaterial (the  $y$ -axis) when it is charged at  $j = 80.0 \text{ A g}^{-1}$  and the total charge (the  $x$ -axis also corresponds to the charging time). In the case of  $E_{\text{cut-off, ch}} = 1.50 \text{ V}$ , the results lead to the following observations: 1) the anodic peak associated with the oxidation of  $\beta$ -Ni(OH)<sub>2</sub> shifts toward higher potentials, its current increases, and the OER is enhanced (Figure 10b); 2) the cathodic peak corresponding to the reduction of  $\beta$ -NiOOH shifts toward higher potentials, its current decreases pointing to a decrease in the specific capacity of the nanomaterial; and 3) the potential versus total charge

curves (Figure 10d) reveal a decrease in the specific capacity, as they gradually become shorter as the charge–discharge cycle number increases. In the case of the charge–discharge cycling with  $E_{\text{cut-off, ch}} = 1.65 \text{ V}$ , the results lead to the following observations: 1) the anodic peak shifts toward higher potentials, its current decreases, and the OER is enhanced (Figure 10c); 2) the cathodic peak shifts toward higher potentials, its current decreases pointing to a decrease in the specific capacity of the nanomaterial; and 3) the potential versus total charge curves (Figure 10e) reveal a decrease in the specific capacity, as they gradually become shorter as the charge–discharge cycle number increases. In the case of the potential versus total charge curve for  $E_{\text{cut-off, ch}} = 1.65 \text{ V}$ , we observe a plateau at ca.  $E = 1.58 \text{ V}$  (the plateau is more pronounced after 1000 charge–discharge cycles) (Figure 10e). The increase in the total charge with the potential being constant is attributed to the OER—the nanomaterial is entirely oxidized and only the

OER takes place. If the charging continued, then the potential would be expected to increase.

In a separate experiment, we prepared a fresh sample of carbon-supported  $\beta$ -Ni(OH)<sub>2</sub> nanosheets and performed 1000 charge–discharge cycles with  $E_{\text{cut-off,ch}} = 1.50$  V and  $E_{\text{cut-off,dis}} = 1.20$  V and determined the specific capacity to be  $147 \pm 29$  mAh g<sup>-1</sup>. Then, we increased  $E_{\text{cut-off,ch}}$  from 1.50 to 1.65 V and performed a charge–discharge cycle, and then determined the specific capacity to be  $214 \pm 13$  mAh g<sup>-1</sup>. This experiment was conducted to evaluate whether a prior history of charging a sample at  $E_{\text{cut-off,ch}} = 1.50$  V has any impact on its subsequent performance of the nanomaterial at  $E_{\text{cut-off,ch}} = 1.65$  V. The value of  $147$  mAh g<sup>-1</sup> is in excellent agreement with the value reported above. In contrast, the value of  $214$  mAh g<sup>-1</sup> is 21% significantly lower than the value of  $270$  mAh g<sup>-1</sup> reported in Figure 10a, thus for a sample without any history of prior cycling with  $E_{\text{cut-off,ch}} = 1.50$  V. Consequently, the charge retention is 79% of the maximum value that was obtained in the course of research. These results clearly demonstrate that the value of  $E_{\text{cut-off,ch}}$  needs to be carefully selected to obtain the highest values of the specific capacity and cyclability of rechargeable battery material.

#### 2.4. Post Charge–Discharge Cycling Characteristics of the Carbon-Supported $\beta$ -Ni(OH)<sub>2</sub> Nanosheets

To examine the cause of the decrease in the specific capacity of the carbon-supported  $\beta$ -Ni(OH)<sub>2</sub> nanosheets brought about by the repetitive charge–discharge cycling, we performed a TEM analysis to examine any structural and/or morphological changes of the nanomaterial. The treatment involved 1000 charge–discharge cycles with  $E_{\text{cut-off,ch}} = 1.65$  V and  $E_{\text{cut-off,dis}} = 1.20$  V at  $j = 80.0$  A g<sup>-1</sup> in 0.50 M aqueous NaOH solution at  $T = 293$  K. The TEM image (Figure 11a) reveals that the nanomaterial lost its initial unique characteristics (thin, unfolded nanosheets residing on the carbon support; Figure 4b,c) and became partially folded, twisted, and aggregated (Figure 4d,e). Figure 11b,c shows

a graphical representation of the carbon-supported  $\beta$ -Ni(OH)<sub>2</sub> nanosheets prior to and after repetitive charge–discharge cycling. Thus, it is the gradually developing less-organized and distorted structure that gives rise to changes in the CV profiles, new features in the charge–discharge curves, and a reduced specific capacity. In general, nanosheet-structured materials are known to aggregate to minimize their total surface energy.<sup>[50,51]</sup> In the case of freshly-prepared carbon-supported  $\beta$ -Ni(OH)<sub>2</sub> nanosheets, they are anchored (bonded) to the carbon substrate and their location is fixed, thus preventing the nanosheets from undergoing aggregation. It is important to add that the carbon support experiences potentials high enough to undergo oxidation and the process gives rise to a materials loss and an increase in its surface roughness.<sup>[52,53]</sup> The change in the surface morphology of the carbon support also has a significant impact on the structure of the interface between the  $\beta$ -Ni(OH)<sub>2</sub> nanosheets and the carbon support, because it decreases the number of anchoring sites and weakens the overall bond between these two materials. Consequently, the  $\beta$ -Ni(OH)<sub>2</sub> nanosheets gradually lose their attachment to the surface of the carbon support and the loosely-attached nanosheets can 1) undergo agglomeration on the surface of the carbon support; 2) reposition to new site and then agglomerate with other nanosheets; and 3) some  $\beta$ -Ni(OH)<sub>2</sub> nanosheets can become completely detached from the carbon support. To improve the stability of the carbon-supported  $\beta$ -Ni(OH)<sub>2</sub> nanosheets, it is possible to modify the bond strength of the anchoring sites by employing nitrogen-doped carbon material. In addition, an application of highly graphitized carbon materials, such as carbon nanotubes and graphene, is an effective approach to enhance the stability, because they possess remarkable stability due to a lower density of edges and defect sites.<sup>[54]</sup>

The structural and morphological changes within the carbon support and the  $\beta$ -Ni(OH)<sub>2</sub> nanosheets lead to a loss of the surface area and modify the pathways for the transport of electrons and protons within the nanosheets (it is a consequence of the decrease in the number of anchoring sites). It is proposed that

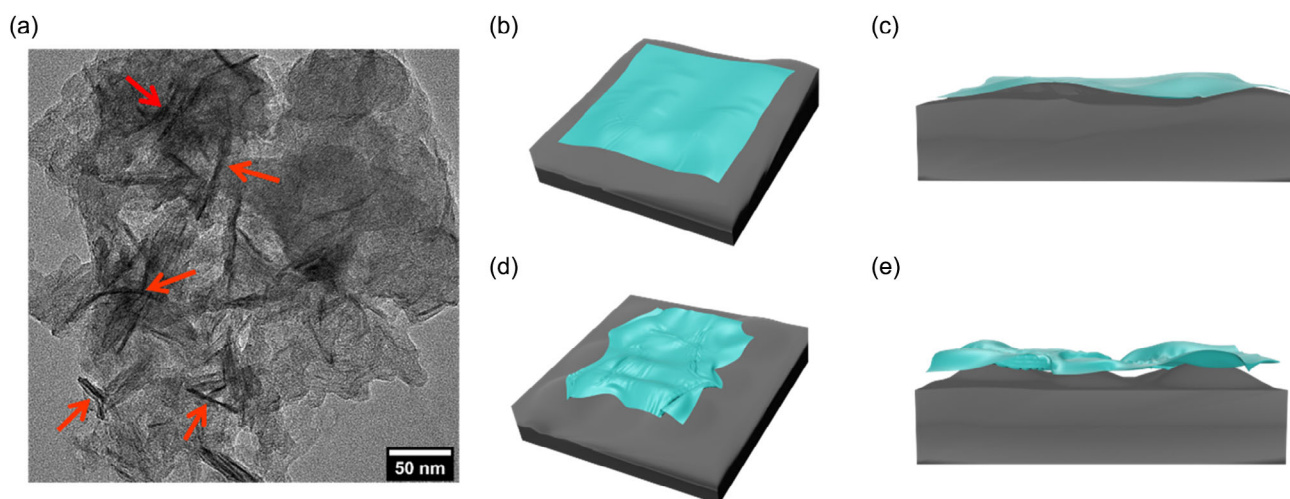


**Figure 11.** TEM image of the carbon-supported  $\beta$ -Ni(OH)<sub>2</sub> nanosheets after repetitive charge–discharge cycling (the graph a, the red arrows indicate the presence of aggregated  $\beta$ -Ni(OH)<sub>2</sub> nanosheets). The treatment involved 1000 charge–discharge cycles with  $E_{\text{cut-off,ch}} = 1.65$  V and  $E_{\text{cut-off,dis}} = 1.20$  V at  $j = 80.0$  A g<sup>-1</sup> in 0.50 M aqueous NaOH solution at  $T = 293$  K. Visual representation of the carbon-supported  $\beta$ -Ni(OH)<sub>2</sub> nanosheets prior to (graphs b) and after (graphs d) the charge–discharge cycling. The graphs c,e) are side views of the graphs b,d), respectively.

these changes in the materials properties are responsible for the modification of the charging–discharging behavior and the loss of the specific capacity of the carbon-supported  $\beta$ -Ni(OH)<sub>2</sub> nanosheets. The loss of specific capacity can also be related to the detachment of some  $\beta$ -Ni(OH)<sub>2</sub> nanosheets from the carbon support (Figure 11e) that no longer participate in the interconversions between  $\beta$ -Ni(OH)<sub>2</sub> and  $\beta$ -NiOOH. Thus, in summary, we attribute the decrease in the specific capacity of the carbon-supported  $\beta$ -Ni(OH)<sub>2</sub> nanosheets to the structural and morphological changes occurring within the nanomaterial and the support during the repetitive charge–discharge cycling.

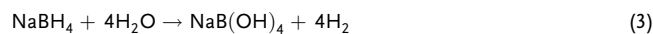
### 3. Conclusion

In summary, a water-in-oil microemulsion method was successfully employed to prepare thin and unfolded  $\beta$ -Ni(OH)<sub>2</sub> on a carbon support. The carbon-supported  $\beta$ -Ni(OH)<sub>2</sub> nanosheets were characterized using TEM, XRD, TGA, and electrochemical techniques (CV, CP, and charge–discharge cycling). The TEM analysis demonstrated that the freshly prepared nanomaterial consisted of thin and unfolded  $\beta$ -Ni(OH)<sub>2</sub> nanosheets residing on the carbon support. XRD characterization showed that the nanosheets were made of  $\beta$ -Ni(OH)<sub>2</sub> without any NiO, which is known to develop in the case of  $\beta$ -Ni(OH)<sub>2</sub> NPs; the  $\beta$ -Ni(OH)<sub>2</sub> nanosheets possessed a hexagonal crystallographic structure. CP (1000 charge–discharge cycles) experiments in aqueous NaOH solution were conducted using two charge cut-off potentials,  $E_{\text{cut-off,ch}} = 1.50$  and  $E_{\text{cut-off,ch}} = 1.65$  V, and one discharge cut-off potential,  $E_{\text{cut-off,dis}} = 1.20$  V. The utilization of the freshly-prepared carbon-supported  $\beta$ -Ni(OH)<sub>2</sub> nanosheets for electrochemical energy storage was 81.5%. The high charge storage capacity was attributed to the sheet-shaped structure of  $\beta$ -Ni(OH)<sub>2</sub> and its good electrical contact to the underlying carbon support. By comparison, the utilization of carbon-supported  $\beta$ -Ni(OH)<sub>2</sub> NPs having an average size of 2.6 nm for electrochemical energy storage was 61%, thus significantly lower despite the NPs having a very good contact with the carbon support and the electrolyte solution.<sup>[37]</sup> The CP transients facilitated a comprehensive analysis of the specific capacity and stability of the nanomaterial upon repetitive potential cycling and revealed that it maintained 54% of its initial charge storage capacity in the case of  $E_{\text{cut-off,ch}} = 1.50$  V and 43% in the case of  $E_{\text{cut-off,ch}} = 1.65$  V. In the case of the carbon-supported  $\beta$ -Ni(OH)<sub>2</sub> NPs, they maintained 95% of their initial charge storage capacity, as examined using CV in the 0.05–1.65 V range at  $s = 50.0$  mV s<sup>-1</sup>.<sup>[32]</sup> Although the  $\beta$ -Ni(OH)<sub>2</sub> nanosheets and the  $\beta$ -Ni(OH)<sub>2</sub> NPs had very similar metal loadings (28% and 27%, respectively) and the same amount of nanomaterial was deposited on glassy carbon electrodes (100  $\mu\text{g cm}^{-2}$ ), their long-term stability was analyzed using different methods, namely CP and CV. Thus, it is difficult to make a direct comparison of the charge storage capacities of these two nanomaterials, although the results demonstrate their remarkable potential in electrochemical energy storage. Because even the purest NaOH is known to contain trace amounts of Fe and because it is known to enhance the kinetics of the OER, repetitive charge–discharge cycling was performed in unpurified and deliberately purified aqueous NaOH solutions. The results demonstrated that the variation of the specific capacity of the

nanomaterial was identical in both electrolyte solutions. In addition, the charge and discharge curves in these electrolyte solutions exhibited the same shape, thus indicating that the presence of trace amounts of Fe in unpurified aqueous NaOH solution had no impact on the redox behavior of the carbon-supported  $\beta$ -Ni(OH)<sub>2</sub> nanosheets. A TEM analysis of the nanomaterial subjected to the repetitive charge–discharge cycling revealed that it developed less-organized and distorted structure. Consequently, it is concluded that this new, less-organized structure gives rise to the loss of specific capacity (loss of charge storage capacity) of the nanomaterial. The structure and electrochemical behavior of nickel hydroxide nanomaterials are very important for their eventual applications in electrochemical energy storage systems. This contribution describes a new research direction and presents new results and their detailed interpretation. It is expected to facilitate the design, development, and optimization of efficient and stable  $\beta$ -Ni(OH)<sub>2</sub> nanomaterials for miniaturized nickel–metal hydride batteries, and possibly even for other applications.

### 4. Experimental Section

*Preparation of Unsupported  $\beta$ -Ni(OH)<sub>2</sub> NPs and Carbon-Supported  $\beta$ -Ni(OH)<sub>2</sub> Nanosheets:* Unsupported  $\beta$ -Ni(OH)<sub>2</sub> NPs were synthesized in a microemulsion solution that was composed of a water–oil mixture and a surfactant.<sup>[37,55]</sup> 34.26 g of n-heptane (Sigma-Aldrich, HPLC grade) and 1.6 mL of 0.20 M nickel precursor aqueous solution were homogeneously mixed with 19.02 g of polyethylene glycol dodecyl ether (Brij L4, Sigma-Aldrich). The nickel precursor aqueous solution was prepared by dissolving nickel (II) chloride hexahydrate (99.999%, Sigma-Aldrich) in UHP water (Milli Q, Millipore, 18.2 M $\Omega$  cm in resistivity). Sodium borohydride (99%, Sigma-Aldrich) in an excess amount (200 mg) was used as a reducing reagent for the formation of  $\beta$ -Ni(OH)<sub>2</sub> NPs. The resulting suspension was allowed to rest for 2 h to ensure that all the nickel precursor had reacted with the reducing reagent (Equation (3) and (4)). Subsequently, the suspension was mixed with acetone (HPLC grade, Fisher Chemical) to remove the oil phase and the surfactant. Once the NPs precipitated, the supernatant was carefully removed. The cleaning was conducted by using acetone three times and then isopropanol also three times (HPLC grade, Sigma-Aldrich). Afterward, the synthesized  $\beta$ -Ni(OH)<sub>2</sub> NPs were stored in isopropanol (HPLC grade, Sigma-Aldrich).



To synthesize carbon-supported  $\beta$ -Ni(OH)<sub>2</sub> nanosheets, a suspension of as-prepared  $\beta$ -Ni(OH)<sub>2</sub> NPs was homogeneously mixed with a predetermined amount of carbon black (Vulcan XC72, CABOT) under sonication for 15 min. The amount of carbon black was calculated to achieve a 30 wt% of nickel loading. Prior to use, carbon black was thermally pretreated in the presence of N<sub>2</sub>(g) at 673 K (400 °C) for 4 h. Acetone was added to the suspension of the carbon-supported  $\beta$ -Ni(OH)<sub>2</sub> nanosheets and filtered using a hydrophilic polyvinylidene difluoride membrane (Millipore) with a 0.22  $\mu\text{m}$  pore diameter. Subsequently, the collected sample was rinsed with HPLC-grade acetone several times. The rinsing was also conducted using HPLC-grade ethanol and UHP water, respectively. After the cleaning step, the sample was dried overnight at 343 K (70 °C), followed by a heat treatment in air for 2 h at 473 K (200 °C) to completely remove trace amounts of remaining surfactant. The steps involved in the synthesis of the unsupported  $\beta$ -Ni(OH)<sub>2</sub> NPs and the carbon-supported  $\beta$ -Ni(OH)<sub>2</sub> nanosheets are presented in the flow chart (Figure 12).

*Physicochemical Characterization:* The TGA was employed to analyze the chemical composition of the carbon-supported  $\beta$ -Ni(OH)<sub>2</sub> nanosheets

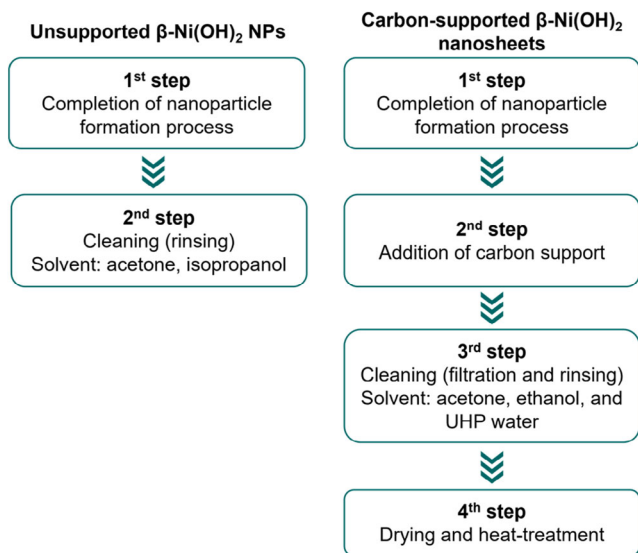


**Figure 12.** A flow chart summarizing the steps involved in the synthesis of the unsupported  $\beta\text{-Ni(OH)}_2$  NPs and the carbon-supported  $\beta\text{-Ni(OH)}_2$  nanosheets.

and to determine the actual material loading using a TA Instrument model TGA Q 500 apparatus. The analysis was conducted in the 25 to 900 °C range at a heating rate of 10 °C min<sup>-1</sup> in air with a flow rate of 100 mL min<sup>-1</sup>. The XRD patterns were recorded in the 2 $\theta$  range from 10° to 90° in a step mode with a 0.06° step at 10 s per step of a fixed acquisition time using Bruker D2 Phaser diffractometer with Cu K $\alpha$  radiation (1.54184 Å). The Levenberg–Marquardt method was employed to deconvolute XRD patterns with a pseudo-Voigt fitting using the Fityk software. The structure and morphology of the unsupported  $\beta\text{-Ni(OH)}_2$  NPs and the carbon-supported  $\beta\text{-Ni(OH)}_2$  nanosheets were analyzed using TEM (Talos F200i instrument, Thermo Fisher Scientific); the nanomaterials were deposited on a carbon-coated Cu 300-mesh grid. In the case of the unsupported  $\beta\text{-Ni(OH)}_2$  NPs, the deposited sample on the TEM grid was subjected to plasma cleaning for 30 s using a model 1020 plasma cleaner apparatus (Fischione Instruments).

**Electrochemical Measurements:** The electrochemical measurements were conducted using a three-electrode electrochemical cell at room temperature ( $T = 293 \pm 1$  K). The working electrode (WE) was comprised of the carbon-supported  $\beta\text{-Ni(OH)}_2$  nanosheets deposited on a glassy-carbon disk (3.00 mm in diameter), which was embedded in a Teflon sleeve. The surface of the glassy-carbon disk was polished to a mirror-like finish prior to each experiment, and 3.00  $\mu\text{L}$  of a sample ink was dropcast on it. The nickel loading of the carbon-supported  $\beta\text{-Ni(OH)}_2$  nanosheets was 100  $\mu\text{g cm}^{-2}$  after drying with N<sub>2</sub>(g) (99.999%, Praxair). To prepare the sample ink, 23.56 mg of the carbon-supported  $\beta\text{-Ni(OH)}_2$  nanosheets were homogeneously dispersed in a mixture of 258  $\mu\text{L}$  of Na $\text{fion}$  solution (5 wt% in lower aliphatic alcohols, Sigma-Aldrich) and 2742  $\mu\text{L}$  of isopropanol (99.5%, Sigma-Aldrich) under sonication for 5 min. The sample ink was dried with N<sub>2</sub>(g) (99.999% in purity, Praxair) stream. A glassy-carbon plate and a reversible hydrogen electrode (RHE) were used as counter and reference electrodes, respectively.

The electrochemical properties of the carbon-supported  $\beta\text{-Ni(OH)}_2$  nanosheets were investigated in 0.50 M aqueous NaOH solution outgassed with N<sub>2</sub>(g). The electrolyte was prepared using sodium hydroxide monohydrate (NaOH·H<sub>2</sub>O, 99.996%, Alfa Aesar) and UHP water. Because even very pure NaOH may contain trace amounts of Fe and because Fe incorporated into  $\beta\text{-Ni(OH)}_2$  may modify its electrocatalytic properties, we also prepared a purified NaOH solution. The details of the purification procedure are reported elsewhere,<sup>[49]</sup> but we modified it slightly because we used NaOH while the cited authors employed KOH. The purification

methodology employed is as follows. A nickel nitrate solution was prepared by dissolving 0.600 g of nickel (II) nitrate hexahydrate (Ni(NO<sub>3</sub>)<sub>2</sub>·H<sub>2</sub>O, 99.999%, Sigma-Aldrich) in 1.50 mL of UHP water. This solution was mixed with 12.0 mL of 0.50 M aqueous NaOH solution to precipitate nickel hydroxide and then centrifuged for 5 min at 3000 revolutions per minute (rpm). After the supernatant was removed, the nickel hydroxide precipitate was rinsed with a mixture of 2.00 mL of 0.50 M aqueous NaOH solution and 10.0 mL of UHP water. The resulting suspension was then centrifuged for 5 min at 3000 rpm. The rinsing and centrifugation steps were repeated three times. Finally, the nickel hydroxide was added to a freshly prepared 0.50 M aqueous NaOH solution and, as it precipitated, traces of Fe were removed from the NaOH solution (most likely also precipitated). The mixture of the nickel hydroxide precipitate and the aqueous alkaline solution was left for 24 h. Prior to the use of the aqueous NaOH solution for electrochemical measurements, the nickel hydroxide containing trace amounts of Fe impurities was removed by centrifugation at 5000 rpm for 10 min.

To examine the behavior of the redox interconversions between  $\beta\text{-Ni(OH)}_2$  and  $\beta\text{-NiOOH}$  in aqueous alkaline solution, CV measurements were performed between  $E = 0.10$  V and  $E = 1.60$  V at a potential scan rate of  $s = 20.0$  mV s<sup>-1</sup> with the WE being rotated at 1600 rpm to remove oxygen gas generated at the electrode's surface in the OER potential region. The charge–discharge behavior of the carbon-supported  $\beta\text{-Ni(OH)}_2$  nanosheets was investigated by CP measurements at various constant current densities in the  $j = 0.500\text{--}20.0$  A g<sup>-1</sup> range. To examine the stability of the nanomaterial, repetitive charge–discharge cycling was conducted at  $j = 80.0$  A g<sup>-1</sup> with  $E_{\text{cut-off, ch}} = 1.50$  V or  $E_{\text{cat-off, ch}} = 1.65$  V for the charge and  $E_{\text{cut-off, dis}} = 1.20$  V. In the case of the charge–discharge measurements with  $E_{\text{cut-off, ch}} = 1.65$  V, the WE was rotated at 1600 rpm for 30 s after every 100 charge–discharge cycles.

## Acknowledgements

This research was conducted as part of the Engineered Nickel Catalysts for Electrochemical Clean Energy project administered from Queen's University and supported by grant no. RGNM 477963-2015 under the Natural Sciences and Engineering Research Council of Canada (NSERC) Discovery Frontiers Program. S.F. gratefully acknowledges financial support for international travel from the Mitacs Globalink Research Award. S.B. and C.C. acknowledge support toward their international travel from the “Ni Electro Can” project. The authors thank Dr. Kevin McEleney at Queen's University for his support to conduct TEM analyses and Dr. Peng Wang for the generous offer to use the X-ray Diffractometer in his group.

## Conflict of Interest

The authors declare no conflict of interest.

## Author Contributions

The manuscript was written through contributions of all authors. All authors have given approval to the final version of the manuscript.

## Data Availability Statement

The data that support the findings of this study are available from the corresponding author upon reasonable request.

## Keywords

beta-nickel hydroxide nanosheets, charge–discharge capacity, miniaturized energy storage applications, nanosheets, nickel–metal hydride batteries, stability



Received: October 10, 2023  
Revised: December 11, 2023  
Published online:

- [1] S. Chu, Y. Cui, N. Liu, *Nat. Mater.* **2016**, *16*, 16.
- [2] S. C. Roy, O. K. Varghese, M. Paulose, C. A. Grimes, *ACS Nano* **2010**, *4*, 1259.
- [3] S. Singh, S. Jain, V. Ps, A. K. Tiwari, M. R. Nouni, J. K. Pandey, S. Goel, *Renewable Sustainable Energy Rev.* **2015**, *51*, 623.
- [4] P. Zhang, F. Wang, M. Yu, X. Zhuang, X. Feng, *Chem. Soc. Rev.* **2018**, *47*, 7426.
- [5] H. Jia, Z. Wang, B. Tawiah, Y. Wang, C. Y. Chan, B. Fei, F. Pan, *Nano Energy* **2020**, *70*, 104523.
- [6] K. Amine, R. Kanno, Y. Tzeng, *MRS Bull.* **2014**, *39*, 395.
- [7] K. H. Young, S. Yasuoka, *Batteries* **2016**, *2*, 3.
- [8] W. Chen, Y. Jin, J. Zhao, N. Liu, Y. Cui, *Proc. Natl. Acad. Sci. U. S. A.* **2018**, *115*, 11694.
- [9] Y. Jiang, C. Zhou, J. Liu, *Energy Storage Mater.* **2018**, *11*, 75.
- [10] D. Kong, Y. Wang, S. Huang, B. Zhang, Y. Von Lim, G. J. Sim, P. Valdivia, Y. Alvarado, Q. Ge, H. Y. Yang, *ACS Nano* **2020**, *14*, 9675.
- [11] Y. Jiao, J. Pei, C. Yan, D. Chen, Y. Hu, G. Chen, *J. Mater. Chem. A* **2016**, *4*, 13344.
- [12] Y. Zeng, Y. Meng, Z. Lai, X. Zhang, M. Yu, P. Fang, M. Wu, Y. Tong, X. Lu, *Adv. Mater.* **2017**, *29*, 1702698.
- [13] A. Van Der Ven, D. Morgan, Y. S. Meng, G. Ceder, *J. Electrochem. Soc.* **2006**, *153*, A210.
- [14] D. S. Hall, D. J. Lockwood, C. Bock, B. R. MacDougall, *Proc. R. Soc. A* **2015**, *471*, 20140792.
- [15] P. Oliva, J. Leonardi, J. F. Laurent, C. Delmas, J. J. Braconnier, M. Figlarz, F. Fievet, A. Guibert, *J. Power Sources* **1982**, *8*, 229.
- [16] H. Bode, K. Dehmelt, J. Witte, *Electrochim. Acta* **1966**, *11*, 1079.
- [17] R. A. Huggins, H. Prinz, M. Wohlfahrt-Mehrens, L. Jörisen, W. Witschel, *Solid State Ionics* **1994**, *70–71*, 417.
- [18] Q. Wang, Y. Li, C. Zhang, *J. Electrochem. Soc.* **2021**, *168*, 076502.
- [19] Z. Wu, T. Wang, J. J. Zou, Y. Li, C. Zhang, J. J. Zou, C. Zhang, *ACS Catal.* **2022**, *12*, 5911.
- [20] L. Zhao, Y. Li, C. Zhang, *J. Energy Storage* **2023**, *65*, 107303.
- [21] Z. Tang, C. H. Tang, H. Gong, *Adv. Funct. Mater.* **2012**, *22*, 1272.
- [22] X. Li, C. Guan, Y. Hu, J. Wang, *ACS Appl. Mater. Interfaces* **2017**, *9*, 26008.
- [23] Y. Wang, X. Zhu, J. Qin, Z. Wang, Y. Wu, Z. Man, C. Yuan, Z. Lü, *J. Electrochem. Soc.* **2021**, *168*, 030523.
- [24] X. Shi, J. Key, S. Ji, V. Linkov, F. Liu, H. Wang, H. Gai, R. Wang, *Small* **2019**, *15*, 1802861.
- [25] H. J. Lo, M. C. Huang, Y. H. Lai, H. Y. Chen, *Mater. Chem. Phys.* **2021**, *262*, 124306.
- [26] Y. Tang, Y. Liu, S. Yu, W. Guo, S. Mu, H. Wang, Y. Zhao, L. Hou, Y. Fan, F. Gao, *Electrochim. Acta* **2015**, *161*, 279.
- [27] D. Wang, C. Song, Z. Hu, X. Fu, *J. Phys. Chem. B* **2005**, *109*, 1125.
- [28] X. Yi, H. Sun, N. Robertson, C. Kirk, *Sustainable Energy Fuels* **2021**, *5*, 5236.
- [29] S. Yang, X. Wu, C. Chen, H. Dong, W. Hu, X. Wang, *Chem. Commun.* **2012**, *48*, 2773.
- [30] H. Wang, J. T. Robinson, G. Diankov, H. Dai, *J. Am. Chem. Soc.* **2010**, *132*, 3270.
- [31] Z. H. Liang, Y. J. Zhu, X. L. Hu, *J. Phys. Chem. B* **2004**, *108*, 3488.
- [32] T. Chen, Y. Bai, X. Xiao, H. Pang, *Chem. Eng. J.* **2021**, *413*, 127523.
- [33] W. Sun, X. Rui, M. Ulaganathan, S. Madhavi, Q. Yan, *J. Power Sources* **2015**, *295*, 323.
- [34] Y. Zhu, C. Cao, S. Tao, W. Chu, Z. Wu, Y. Li, *Sci. Rep.* **2014**, *4*, 5787.
- [35] M. Jiang, Y. Zhu, Y. Liu, J. Zhang, Y. Zhang, Y. Sun, P. Zeng, J. Hou, Y. Ren, Z. Ba, L. Li, *J. Alloys Compd.* **2023**, *941*, 168980.
- [36] Y. Liu, J. Yu, M. Jiang, J. Hou, Y. Zhu, J. Zhang, Z. Ba, L. Li, *Int. J. Hydrogen Energy* **2022**, *47*, 41087.
- [37] S. Tahmasebi, S. Jahangiri, N. Mosey, G. Jerkiewicz, A. Mark, S. Cheng, G. Botton, S. Baranton, C. Coutanceau, *ACS Appl. Energy Mater.* **2020**, *3*, 7294.
- [38] A. Zalineeva, S. Baranton, C. Coutanceau, G. Jerkiewicz, *Sci. Adv.* **2017**, *3*, e1600542.
- [39] P. Muthu, K. Sinnaeruvadi, *Mater. Chem. Phys.* **2021**, *274*, 125129.
- [40] K. Nishimura, T. Takasaki, T. Sakai, *J. Alloys Compd.* **2013**, *580*, S353.
- [41] H. Uesato, H. Miyaoka, T. Ichikawa, Y. Kojima, *Int. J. Hydrogen Energy* **2019**, *44*, 4263.
- [42] W. Liu, R. Yin, W. Shi, X. Xu, X. Shen, Q. Yin, L. Xu, X. Cao, *ACS Appl. Energy Mater.* **2019**, *2*, 579.
- [43] L. Yu, P. Pellechia, M. A. Matthews, *Int. J. Hydrogen Energy* **2014**, *39*, 442.
- [44] M. Wojdyr, *J. Appl. Crystallogr.* **2010**, *43*, 1126.
- [45] A. K. Mondal, D. Su, S. Chen, B. Sun, K. Li, G. Wang, *RSC Adv.* **2014**, *4*, 19476.
- [46] S. A. Abbas, M. I. Iqbal, S. H. Kim, H. Abbas Khan, K. D. Jung, *Appl. Surf. Sci.* **2019**, *474*, 218.
- [47] M. Alsabet, M. Grdeń, G. Jerkiewicz, *Electrocatalysis* **2014**, *6*, 60.
- [48] G. W. Yang, C. L. Xu, H. L. Li, *Chem. Commun.* **2008**, *28*, 6537.
- [49] L. Trotochaud, S. L. Young, J. K. Ranney, S. W. Boettcher, *J. Am. Chem. Soc.* **2014**, *136*, 6744.
- [50] C. Zhang, J. Zhao, L. Zhou, Z. Li, M. Shao, M. Wei, *J. Mater. Chem. A* **2016**, *4*, 11516.
- [51] Y. Zhao, Y. Zhao, G. I. N. Waterhouse, L. Zheng, X. Cao, F. Teng, L. Z. Wu, C. H. Tung, D. O'Hare, T. Zhang, *Adv. Mater.* **2017**, *29*, 1703828.
- [52] A. Zadick, L. Dubau, N. Sergent, G. Berthomé, M. Chatenet, *ACS Catal.* **2015**, *5*, 4819.
- [53] L. Castanheira, L. Dubau, M. Mermoux, G. Berthomé, N. Caqué, E. Rossinot, M. Chatenet, F. Maillard, *ACS Catal.* **2014**, *4*, 2258.
- [54] I. C. Gerber, P. Serp, *Chem. Rev.* **2020**, *120*, 1250.
- [55] S. Baranton, C. Coutanceau, *Appl. Catal., B* **2013**, *136–137*, 1.